



Deposited via The University of Sheffield.

White Rose Research Online URL for this paper:

<https://eprints.whiterose.ac.uk/id/eprint/146797/>

Version: Accepted Version

Article:

Wu, L.J., Li, Z., Wang, D. et al. (2019) On-load field prediction of surface-mounted PM machines considering nonlinearity based on hybrid field model. IEEE Transactions on Magnetics, 55 (3). 8100911. ISSN: 0018-9464

<https://doi.org/10.1109/TMAG.2018.2890244>

© 2019 IEEE. Personal use of this material is permitted. Permission from IEEE must be obtained for all other users, including reprinting/ republishing this material for advertising or promotional purposes, creating new collective works for resale or redistribution to servers or lists, or reuse of any copyrighted components of this work in other works. Reproduced in accordance with the publisher's self-archiving policy.

Reuse

Items deposited in White Rose Research Online are protected by copyright, with all rights reserved unless indicated otherwise. They may be downloaded and/or printed for private study, or other acts as permitted by national copyright laws. The publisher or other rights holders may allow further reproduction and re-use of the full text version. This is indicated by the licence information on the White Rose Research Online record for the item.

Takedown

If you consider content in White Rose Research Online to be in breach of UK law, please notify us by emailing eprints@whiterose.ac.uk including the URL of the record and the reason for the withdrawal request.

On-Load Field Prediction of Surface-Mounted PM Machines Considering Nonlinearity Based on Hybrid Field Model

L. J. Wu¹, Senior Member IEEE, Zhaokai Li¹, Dong Wang², Member IEEE, Hao Yin¹, Xiaoyan Huang¹, Member IEEE, and Z. Q. Zhu³, Fellow IEEE

¹College of Electrical Engineering, Zhejiang University, Hangzhou, 310027 China

²National Key Laboratory of Science and Technology on Vessel Integrated Power System
Naval Univ. of Engineering, 430000, Wuhan, China

³Department of Electronic and Electrical Engineering, University of Sheffield, Sheffield S1 3JD, U.K.

Analytical models show weakness in dealing with saturation in surface-mounted PM (SPM) machines. A hybrid field model (HFM) integrating complex permeance method (CPM) and lumped parameter magnetic circuit model (LPMCM) is proposed in this paper for predicting the on-load magnetic field considering nonlinearity effect of stator lamination. In the proposed model, the CPM calculates the field in the airgap and magnet regions, while LPMCM calculates the magnetic potential distribution inside iron reflecting nonlinearity effect. The equivalent current sheet is obtained to replace such distribution on the stator bore. Moreover, local magnetic saturation of tooth-tip is also transformed into equivalent current on the tooth surface. A solving procedure is proposed to calculate the equivalent current and guarantee the convergence. Compared with CPM, the proposed model considering saturation effect significantly improves the prediction accuracy of the on-load performance. The HFM predictions are compared with finite element (FE) and experimental results. The excellent agreement validates its effectiveness.

Index Terms—Analytical model, magnetic equivalent circuit, complex permeance, saturation effect, SPM machines.

I. INTRODUCTION

PERMANENT-MAGNET (PM) machines become increasingly popular benefiting from their high torque density and efficiency [1]. Therefore, researchers have made great effort in developing accurate and fast tools for analysis, design and optimization of such machines. Although numerical methods are accurate, it is very time-consuming and provides little straightforward physical insight into machine design [2]. On the contrary, many analytical models are available to quickly reveal the physical relationship between the geometry of PM machines and their performance [3]-[9]. They are accurate for machines with linear materials. However, machine designers usually push work point of iron material to or slightly over the knee point of its BH curve in order to achieve better torque density. Hence, the analytical models lack of high accuracy for these machines because of neglecting nonlinearity effect.

The preference of both high computational speed and accuracy motivates the integration of analytical models with numerical methods. There are many potential candidates for such integration. For analytical models, complex permeance model is a good option. Zhu *et al.* analytically calculated the field in the airgap/magnet regions for slotless PM machines in [3]-[4]. The stator slotting effect can be taken into account by conformal mapping. Typical examples can be found in [5], which gives calculation of complex permeance function to consider slotting effect on both radial and circumferential components of flux density. It is simple and fast because Schwarz-Christoffel (SC) transformation is required only once, but it neglects the deformation of magnets and path for airgap

field prediction. To eliminate this error, exact conformal mapping based on SC Toolbox can be used to accurately calculate the magnetic field in the SPM machines [7]-[8]. SC Toolbox was developed to construct a SC map from the machine geometry at first and then numerically evaluate the position of PM equivalent current in the canonical domain at every rotor position [10]. Hence, it is very time-consuming. On the other hand, the LPMCM is a good option for numerical method since both finite element and finite difference methods requires large calculation and are not preferred. The LPMCM is fast and very effective for the path in the iron, but often shows difficulty for the path in the air. It is because the flux tube in the air has complicated shape, which can be varying with the rotor position [11]-[12]. It is particularly difficult for the airgap and magnet regions in SPM machines, in which the surface of magnet does not show equal potential. The area of LPMCM's weakness is exactly the strong side of analytical models. Therefore, the integration of CPM and LPMCM can provide both high computational speed and accuracy.

In order to account for iron nonlinearity, some analytical models are modified to account for the magnetic potential distribution in the iron. Dalal *et al.* obtained the airgap field distribution by solving Laplace/quasi-Poissonian equations in six regions, of which the stator core permeability is assumed a linear function of the load angle [13]. However, such linear function is found by using finite element method (FEM) and the whole stator iron is assumed the constant permeability. On the other hand, LPMCM is often used to analyze the nonlinear iron core. From the LPMCM solution, the airgap length and slot opening are modified to represent the magnetic potential drops of the stator [14]-[16]. Then the complex permeance based on the modified airgap and slot opening was introduced to account for both saturation effect and slotting effect. Nevertheless, these models in [14]-[16] are time-consuming due to the calculation

of the saturated complex permeance using SC transformation at every rotor position.

In addition, equivalent virtual current is powerful in magnetic field calculation. It has been widely used to replace the PM and calculate the electromagnetic performance in many PM machines such as IPM machine [17], transverse flux machine [18], and eccentric SPM machine [19]. For the saturated SPM machine, Hanic *et al.* combined the conformal mapping and LPMCM to analyze the airgap field [20]-[21] by using equivalent currents. The SC mapping in [20] and [21] transforms the slotted domain with equivalent current sheets of magnets into slotless domain. The field distribution due to winding current and magnet equivalent currents placed at the new mapped positions is calculated by using Hague's solution. It is then transformed back into original slotted domain. In [22], the CPM instead of exact conformal mapping in [20]-[21] is combined with LPMCM to predict the open-circuit field of SPM machines, but the analysis of on-load field is not included as well as the consideration of tooth-tip saturation, which is common and important in electric machines. Hence, this paper will investigate on-load field of SPM machines accounting for slot flux leakage. Most importantly, the tooth-tip saturation will be analyzed in this paper.

A HFM integrating CPM and LPMCM is presented for the on-load field prediction in SPM machines with tooth-tips. Such combination is based on the equivalence between the magnetic potential drop in the stator and virtual current along the stator bore. In order to calculate the virtual current representing nonlinearity effect, a solving procedure based on Newton-Raphson method is developed to guarantee the convergence in the iteration. Both FE analysis and experiment are implemented to verify the proposed model.

II. HYBRID FIELD MODEL

Assumptions are made to ease modeling: 1) PM has a linear recoil line; 2) the end effect is neglected; 3) the rotor iron is infinitely permeable. As for some cases that rotor iron saturation cannot be neglected, the model should be reconstructed.

Fig. 1 shows the schematic view of SPM machine; whose stator iron has a nonlinear permeability. When different level of excitation from PM and winding current is applied, there will be different work point of stator iron on the BH curve, viz. different relative permeability μ_{r_stator} . Since the analytical model is not applicable to the nonlinear model in Fig. 1, it has to be equivalently transformed into an infinitely permeable model, whose magnetic potential drop in the stator becomes zero. In order to compensate the magnetic potential drop in the stator of infinitely permeable model, virtual equivalent current is introduced to represent the nonlinearity effect, as shown in Fig. 2. It is noted that the virtual current at the slot opening is used to consider the saturation of stator yoke and teeth body while the virtual current at the teeth surface is presented to show the tooth-tip saturation. Fig. 3 shows the justification of introducing the virtual current. Along the loop 1 in Fig.3(a), the Ampere' law can be applied as:

$$F_{tip1} + \int_{L_{airgap1}} H_{airgap1} dl = 0 \quad (1)$$

where F_{tip1} is the magnetic potential drop across the tooth tip 1, $L_{airgap1}$ is the airgap path of loop 1, and $H_{airgap1}$ is the magnetic field along $L_{airgap1}$.

In Fig.3(b), the Ampere' law can give:

$$0 + \int_{L_{airgap1}} H_{airgap1} dl = i_{tl} \quad (2)$$

In order to keep $H_{airgap1}$ unchanged, the equivalent current should satisfy:

$$i_{tl} = -F_{tip1} \quad (3)$$

Similarly,

$$i_{tr} = -F_{tip2} \quad (4)$$

where i_{tl} and i_{tr} are the equivalent currents at the left and right sides of tooth shoe.

Along the loop 3 in Fig.3(a), according to the Ampere' law:

$$F_{tooth1} + F_{yoke} + F_{tooth2} + \int_{L_{airgap3}} H_{airgap3} dl = NI_w \quad (5)$$

where F_{tooth1} , F_{tooth2} , and F_{yoke} are the magnetic potential drops across the tooth 1, tooth 2 and yoke, respectively, I_w is the winding current and N is the number of turns.

For the same loop in Fig.3(b), the Ampere' law can give:

$$0 + \int_{L_{airgap3}} H_{airgap3} dl = NI_w + i_{tl} + i_{tr} + i_{ss} \quad (6)$$

In order to keep $H_{airgap3}$ unchanged, the equivalent current at the slot opening should be:

$$i_{ss} = -(F_{tooth1} + F_{yoke} + F_{tooth2}) - (i_{tl} + i_{tr}) \quad (7)$$

Hence, the infinitely permeable model can be analytically solved considering iron nonlinearity by equivalent currents.

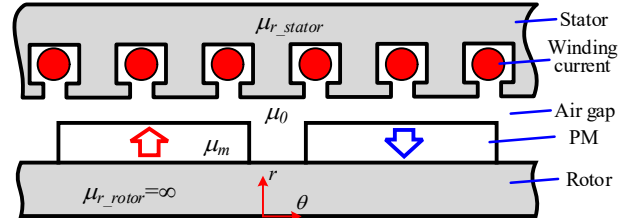


Fig. 1. Schematic view of SPM machine.

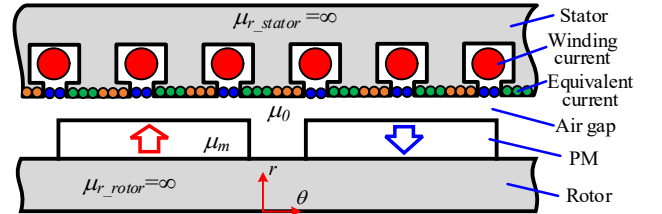


Fig. 2. Hybrid field model of slotted SPM machine considering nonlinearity effect under on-load condition.

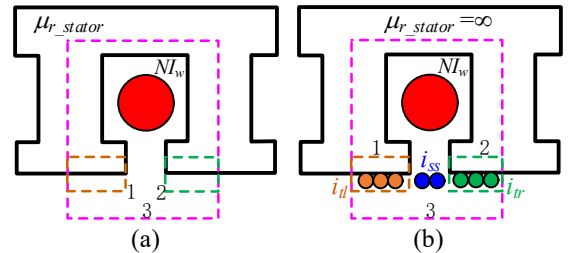


Fig. 3 The Ampere loops in (a) Initial nonlinear model and (b) Equivalent model with equivalent current.

A. Equivalent Current Representing Stator Nonlinearity

The equivalent current, which represents nonlinearity effect, is the keypoint in the HFM. It is calculated from the magnetic potential distribution of LPMCM. Fig. 4 shows that the magnetic reluctances representing the nonlinear property of the stator iron are connected to establish a magnetic network. $V_1, V_2, \dots, V_{(6Q_s)}$ are the node magnetic potential in the LPMCM, where Q_s is the slot number. The airgap flux ϕ_j flowing into the stator is expressed as

$$\phi_j = \int_{s_j} B_{sr}(R_s) ds \quad (8)$$

where s_j is the area of the slot or tooth on the stator bore, j is the index of the slot and tooth ($j=1, 2, \dots, 2Q_s$), R_s is the stator bore radius, and $B_{sr}(R_s)$ is the radial flux density on the stator bore.

According to KCL, the node magnetic potential is obtained by:

$$f(\mathbf{V}) = \mathbf{A}\mathbf{\Lambda}(\mathbf{A}^T\mathbf{V} - \mathbf{E}) - \mathbf{A}\mathbf{\Phi} = 0 \quad (9)$$

where $\mathbf{\Phi}$ is the branch flux matrix which includes ϕ_j for the fluxes into stator and 0 for the rest branches. \mathbf{A} , $\mathbf{\Lambda}$, and \mathbf{V} are the matrixes of the incidence, branch permeance, and node magnetic potential, respectively. The permeance in $\mathbf{\Lambda}$ is calculated using the following equation [11]-[12]:

$$\begin{aligned} p_r &= \frac{\mu l_{ef} a}{b} \\ p_{sr} &= \frac{\mu l_{ef} \alpha_0}{\ln(R_2 / R_1)} \\ p_{st} &= \frac{\mu l_{ef} \ln(R_2 / R_1)}{\alpha_0} \end{aligned} \quad (10)$$

where p_r , p_{sr} , and p_{st} are the permeance of the rectangular material, radial sector material and tangential sector material, respectively. μ is the permeability of the material and l_{ef} is the active length. a is the width of cross-sectional area and b is the length along the flux direction in the rectangle. α_0 , R_1 and R_2 are the central angle, outer radius and inner radius of the sector. It can be seen that p_r is suitable to calculate the tooth permeance in the LPMCM while p_{sr} and p_{st} is intended for the radial and tangential permeance of stator yoke, tooth shoe, slot, and slot-opening. \mathbf{E} is the branch MMF matrix calculated by winding current [11]

$$\begin{cases} E_{2Q_s} = E_{Q_s} = -\frac{1}{2Q_s} \sum_{n=1}^{Q_s-1} (Q_s - n) i_{wn} \\ E_{Q_s+1} = E_1 = E_{Q_s} + \frac{i_{w1}}{2} \\ E_{Q_s+2} = E_2 = E_1 + \frac{i_{w2}}{2} \\ \dots \\ E_{2Q_s-1} = E_{Q_s-1} = E_{Q_s-2} + \frac{i_{w(Q_s-1)}}{2} \end{cases} \quad (11)$$

where $E_1, E_2, \dots, E_{2Q_s}$ are the values of branch MMF which forms \mathbf{E} and $i_{w1}, i_{w2}, \dots, i_{w(Q_s-1)}$ are the winding current.

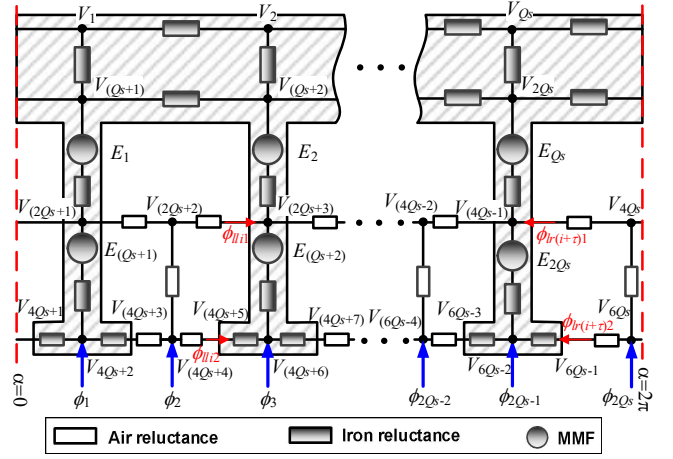


Fig. 4. Equivalent magnetic network of the stator.

The equivalent currents are illustrated in Fig. 5. The equivalent current on the k th slot opening is obtained by:

$$i_{ssk} + i_{wk} = -(V_{m+2} - V_m) \quad (12)$$

where i_{ssk} and i_{wk} are the equivalent and winding currents in the k th slot, respectively, k is the index of tooth and slot, $k=1, 2, \dots, Q_s$, V_m and V_{m+2} are the magnetic potentials of nodes at the left and right sides of the k th slot opening. It is noted that V_{m+2} and V_m in the right side of (12) are calculated from the nonlinear model while i_{ssk} and i_{wk} in the left side of (12) are intended for the infinitely permeable model.

Considering the nonlinearity effect in the tooth-tip, the virtual current on the tooth shoe should be added in the infinitely permeable model. Besides, the virtual current value on the tooth shoe should be equal to the magnetic potential drop along the tooth shoe in order to produce the same airgap field.

$$\begin{cases} i_{tlk} = -(V_{m-1} - V_{m-2}) \\ i_{trk} = -(V_m - V_{m-1}) \end{cases} \quad (13)$$

where i_{tlk} and i_{trk} are the equivalent currents at the left and right sides of the k th tooth shoe, V_{m-1} is the magnetic potential on the node in the middle of the k th tooth top, V_{m-2} and V_m are the magnetic potential on the nodes at the left and right sides of the k th tooth-tip, respectively. Then (12)-(13) can be expressed in the matrix form:

$$\begin{cases} \mathbf{I}_{ss} + \mathbf{I}_w = \mathbf{C}_{ss} \mathbf{V} \\ \mathbf{I}_{tl} = \mathbf{C}_{tl} \mathbf{V} \\ \mathbf{I}_{tr} = \mathbf{C}_{tr} \mathbf{V} \end{cases} \quad (14)$$

where \mathbf{C}_{ss} , \mathbf{C}_{tl} , \mathbf{C}_{tr} are the constant matrixes calculated from (12)-(13) and

$$\mathbf{I}_{ss} = [i_{ss1} \quad i_{ss2} \quad \dots \quad i_{ssQ_s}]^T \quad (15)$$

$$\mathbf{I}_w = [i_{w1} \quad i_{w2} \quad \dots \quad i_{wQ_s}]^T \quad (16)$$

$$\mathbf{I}_{tl} = [i_{tl1} \quad i_{tl2} \quad \dots \quad i_{tlQ_s}]^T \quad (17)$$

$$\mathbf{I}_{tr} = [i_{tr1} \quad i_{tr2} \quad \dots \quad i_{trQ_s}]^T \quad (18)$$

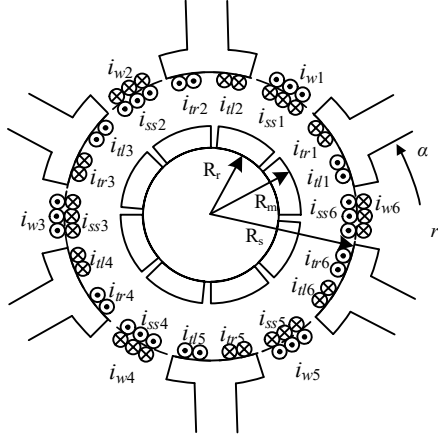


Fig. 5. Illustration of equivalent current sheet.

B. Slotted Airgap Field Solution

Since the equivalent current is introduced to represent the nonlinearity effect, the stator iron becomes infinitely permeable as shown in Fig. 2. Thus, the analytical model with the assumption of infinitely permeable iron is suitable to calculate the magnetic field of SPM machines. As for the slotting effect, CPM based on conformal mapping is used to calculate the slotted airgap field from the slotless airgap field [5].

$$\begin{aligned} B_{sr} &= B_r \lambda_r + B_\alpha \lambda_i \\ B_{s\alpha} &= B_\alpha \lambda_r - B_r \lambda_i \end{aligned} \quad (19)$$

where B_{sr} and $B_{s\alpha}$ are the radial and circumferential slotted airgap flux density, respectively. λ_r and λ_i are the real and imaginary components of complex permeance, whose calculation are described in [22]. B_r and B_α are the radial and circumferential slotless airgap flux density, which are obtained by superposition of the field components produced by the PM, winding and equivalent currents with infinitely permeable iron, Fig. 6.

$$\begin{aligned} B_r(\alpha, r, t) &= B_{mr}(\theta, r) + B_{wr}(\alpha, r, t) + B_{sat_r}(\alpha, r, t) \\ &= B_{mr}(\theta, r) + B_{cr}(\alpha, r, t) \end{aligned} \quad (20)$$

$$\begin{aligned} B_\alpha(\alpha, r, t) &= B_{m\alpha}(\theta, r) + B_{w\alpha}(\alpha, r, t) + B_{sat_a}(\alpha, r, t) \\ &= B_{m\alpha}(\theta, r) + B_{c\alpha}(\alpha, r, t) \end{aligned} \quad (21)$$

where B_{mr} and $B_{m\alpha}$ are the radial and circumferential flux density components due to the PM, B_{wr} and $B_{w\alpha}$ are the radial and circumferential flux density components due to the winding current, B_{sat_r} and B_{sat_a} are the radial and circumferential flux density components due to the equivalent current. α and θ are the stator and rotor angular positions, respectively, and $\theta = \omega_r t + \theta_0$, where θ_0 is the initial position of the rotor and ω_r is the mechanical angular velocity.

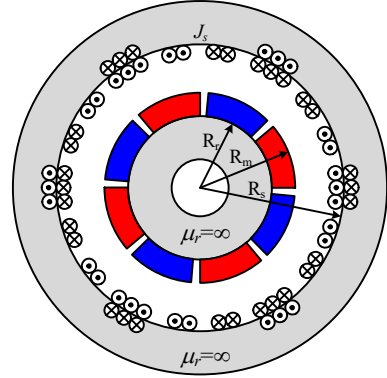


Fig. 6. Hybrid field model of slotless SPM machine.

The solution of the slotless airgap field due to PMs neglecting nonlinearity effect was derived in [22]. Therefore, this paper only gives the final expressions of radial and circumferential airgap flux density components:

$$B_{mr}(\theta, r) = \sum_{n=1,3,5,\dots}^{\infty} K_B(n) f_{Br}(r) \cos(np\theta) \quad (22)$$

$$B_{m\alpha}(\theta, r) = \sum_{n=1,3,5,\dots}^{\infty} K_B(n) f_{B\theta}(r) \sin(np\theta) \quad (23)$$

where $K_B(n)$, $f_{Br}(r)$, and $f_{B\theta}(r)$ are given in [22].

As for the magnetic field produced by stator current including winding current and equivalent current of saturation neglecting saturation effect, the governing Laplacian equation in the airgap region is

$$\frac{\partial^2 \varphi}{\partial r^2} + \frac{1}{r} \frac{\partial \varphi}{\partial r} + \frac{1}{r^2} \frac{\partial^2 \varphi}{\partial \alpha^2} = 0 \quad (24)$$

and the boundary condition is [4]

$$\begin{cases} B_\alpha|_{r=R_r} = 0 \\ H_\alpha|_{r=R_s} = -J_s \end{cases} \quad (25)$$

where R_r is the rotor yoke surface radius and J_s is the resultant of winding and equivalent currents, which can be expressed as Fourier series from Fig. 5

$$\begin{aligned} J_s &= \sum_{k=1}^{Q_s} \sum_v \frac{2(i_{ssk} + i_{wk})}{\pi b_0} \frac{1}{v} \sin\left(\frac{vb_0}{2R_s}\right) \cos\left[v\left(\alpha - \frac{2k\pi}{Q_s}\right)\right] + \\ &\sum_{k=1}^{Q_s} \sum_v \frac{4i_{tk}}{\pi t_0} \frac{1}{v} \sin\left(\frac{vt_0}{4R_s}\right) \cos\left[v\left(\alpha - \frac{(2k-1)\pi}{Q_s} + \frac{t_0}{4R_s}\right)\right] + \\ &\sum_{k=1}^{Q_s} \sum_v \frac{4i_{rk}}{\pi t_0} \frac{1}{v} \sin\left(\frac{vt_0}{4R_s}\right) \cos\left[v\left(\alpha - \frac{(2k-1)\pi}{Q_s} - \frac{t_0}{4R_s}\right)\right] \end{aligned} \quad (26)$$

where b_0 is the slot-opening width and t_0 is the tooth top width.

By solving the governing Laplacian equation with the boundary condition, the radial and circumferential flux density components due to the stator current can be given by:

$$B_{cr} = \frac{\mu_0}{\pi} \sum_{k=1}^{Q_s} \sum_v \left\{ \frac{i_{ssk} + i_{wk}}{v} K_{sov}(b_0) F_v(r) \sin \left[v \left(\alpha - \frac{2k\pi}{Q_s} \right) \right] + \frac{i_{tk}}{v} K_{sov} \left(\frac{t_0}{2} \right) F_v(r) \sin \left[v \left(\alpha - \frac{(2k-1)\pi}{Q_s} + \frac{t_0}{4R_s} \right) \right] + \frac{i_{trk}}{v} K_{sov} \left(\frac{t_0}{2} \right) F_v(r) \sin \left[v \left(\alpha - \frac{(2k-1)\pi}{Q_s} - \frac{t_0}{4R_s} \right) \right] \right\} \quad (27)$$

$$B_{ca} = \frac{\mu_0}{\pi} \sum_{k=1}^{Q_s} \sum_v \left\{ \frac{i_{ssk} + i_{wk}}{v} K_{sov}(b_0) G_v(r) \cos \left[v \left(\alpha - \frac{2k\pi}{Q_s} \right) \right] + \frac{i_{tk}}{v} K_{sov} \left(\frac{t_0}{2} \right) G_v(r) \cos \left[v \left(\alpha - \frac{(2k-1)\pi}{Q_s} + \frac{t_0}{4R_s} \right) \right] + \frac{i_{trk}}{v} K_{sov} \left(\frac{t_0}{2} \right) G_v(r) \cos \left[v \left(\alpha - \frac{(2k-1)\pi}{Q_s} - \frac{t_0}{4R_s} \right) \right] \right\} \quad (28)$$

where F_v , G_v , and K_{sov} are

$$F_v(r) = \frac{v}{r} \left(\frac{r}{R_s} \right)^v \frac{1 + (R_r/r)^{2v}}{1 - (R_r/R_s)^{2v}} \quad (29)$$

$$G_v(r) = \frac{v}{r} \left(\frac{r}{R_s} \right)^v \frac{1 - (R_r/r)^{2v}}{1 - (R_r/R_s)^{2v}} \quad (30)$$

$$K_{sov}(\beta) = \frac{\sin(v\beta/2R_s)}{v\beta/2R_s} \quad (31)$$

C. Convergent Solving Procedure

In the proposed HFM, the airgap field solution and calculation of equivalent current depend on each other. Therefore, a solving procedure is proposed to iteratively calculate the equivalent current as well as airgap field and guarantee the convergence in one loop. The basic idea is to incorporate the airgap analytical solution into the procedure of solving the LPMCM. Therefore, in the LPMCM, the airgap flux φ_j flowing into the stator is rederived from (8)

$$\begin{aligned} \varphi_j &= \sum_{k=1}^{Q_s} \left[g_{ssk}(s_j)(i_{ssk} + i_{wk}) + g_{tlk}(s_j)i_{tk} \right. \\ &\quad \left. + g_{trk}(s_j)i_{trk} \right] + \int_{s_j} (\lambda_r B_{mr} + \lambda_l B_{ma}) ds \\ &= \mathbf{G}_{ss}(s_j)(\mathbf{I}_{ss} + \mathbf{I}_w) + \mathbf{G}_{tl}(s_j)\mathbf{I}_{tl} + \mathbf{G}_{tr}(s_j)\mathbf{I}_{tr} + \varphi_m(s_j) \end{aligned} \quad (32)$$

where g_{ssk} , g_{tlk} , and g_{trk} are calculated from (19)-(31) and

$$\mathbf{G}_{ss}(s_j) = \begin{bmatrix} g_{ss1}(s_j) & g_{ss2}(s_j) & \cdots & g_{ssQ_s}(s_j) \end{bmatrix} \quad (33)$$

$$\mathbf{G}_{tl}(s_j) = \begin{bmatrix} g_{tl1}(s_j) & g_{tl2}(s_j) & \cdots & g_{tlQ_s}(s_j) \end{bmatrix} \quad (34)$$

$$\mathbf{G}_{tr}(s_j) = \begin{bmatrix} g_{tr1}(s_j) & g_{tr2}(s_j) & \cdots & g_{trQ_s}(s_j) \end{bmatrix} \quad (35)$$

$$\varphi_m(s_j) = \int_{s_j} (\lambda_r B_{mr} + \lambda_l B_{ma}) ds \quad (36)$$

The equivalent current $\mathbf{I}_{ss} + \mathbf{I}_w$, \mathbf{I}_{tl} , \mathbf{I}_{tr} in (32) can be calculated from the magnetic potential distribution of LPMCM according to (14). Thus φ_j in (32) is a function of the magnetic potential distribution \mathbf{V} .

$$\varphi_j = (\mathbf{G}_{ss}(s_j)\mathbf{C}_{ss} + \mathbf{G}_{tl}(s_j)\mathbf{C}_{tl} + \mathbf{G}_{tr}(s_j)\mathbf{C}_{tr})\mathbf{V} + \varphi_m(s_j) \quad (37)$$

It can also be expressed in the matrix form as

$$\Phi = (\mathbf{R}_{ss}\mathbf{C}_{ss} + \mathbf{R}_{tl}\mathbf{C}_{tl} + \mathbf{R}_{tr}\mathbf{C}_{tr})\mathbf{V} + \Phi_m \quad (38)$$

where

$$\mathbf{R}_{ss} = \begin{bmatrix} \mathbf{G}_{ss}(s_1) & \mathbf{G}_{ss}(s_2) & \cdots & \mathbf{G}_{ss}(s_{2Q_s}) \end{bmatrix}^T \quad (39)$$

$$\mathbf{R}_{tl} = \begin{bmatrix} \mathbf{G}_{tl}(s_1) & \mathbf{G}_{tl}(s_2) & \cdots & \mathbf{G}_{tl}(s_{2Q_s}) \end{bmatrix}^T \quad (40)$$

$$\mathbf{R}_{tr} = \begin{bmatrix} \mathbf{G}_{tr}(s_1) & \mathbf{G}_{tr}(s_2) & \cdots & \mathbf{G}_{tr}(s_{2Q_s}) \end{bmatrix}^T \quad (41)$$

$$\Phi_m = \begin{bmatrix} \varphi_m(s_1) & \varphi_m(s_2) & \cdots & \varphi_m(s_{2Q_s}) \end{bmatrix}^T \quad (42)$$

Thus, according to (9), the general solution for LPMCM can be obtained by

$$\begin{aligned} f(\mathbf{V}) &= \mathbf{A} \left[\mathbf{A}\mathbf{A}^T - (\mathbf{R}_{ss}\mathbf{C}_{ss} + \mathbf{R}_{tl}\mathbf{C}_{tl} + \mathbf{R}_{tr}\mathbf{C}_{tr}) \right] \mathbf{V} \\ &\quad - \mathbf{A}\mathbf{A}\mathbf{E} - \mathbf{A}\Phi_m = \mathbf{0} \end{aligned} \quad (43)$$

It can be seen from (43) that only branch permeance matrix \mathbf{A} depends on the magnetic potential distribution. Hence only one loop is required to solve the 'new' LPMCM using BH curves. Fig. 7 shows the general flowchart to calculate the equivalent current and airgap flux density. In fact, the essence of HFM is to replace the inaccurate modeling of airgap reluctance in LPMCM with virtual reluctance (\mathbf{R}_{ss} , \mathbf{R}_{tl} , \mathbf{R}_{tr}) and flux source (Φ_m) from the airgap field solution of CPM. Meanwhile, the airgap magnetic network of HFM is also a Norton equivalent circuit compared to the original LPMCM, which proves the validity of the proposed replacement.

D. Speed and Accuracy in Calculation

The tradeoff between speed and accuracy in the calculation of electromagnetic field is an unavoidable issue for researchers to analyze. Thus it is necessary to compare and investigate the speed and accuracy of CPM, FEM, and HFM in the airgap field prediction. CPM neglects the core saturation and requires no iteration process at any rotor position. Therefore, it is fastest but also least accurate compared with other methods. On the contrary, FEM shows the highest accuracy in predicting the magnetic field and therefore is often employed to verify the accuracy of analytical model for the electrical machines [17]-[21]. However, it is also the most time-consuming method because it need to iteratively solve a $N_{jem} \times N_{jem}$ nonlinear matrix, where N_{jem} represents the number of FE nodes and is always very large for accurate calculation. As for HFM, it combines the advantage of both CPM and LPMCM with high speed and great accuracy. Due to considering nonlinear property of iron core, the accuracy of magnetic field prediction is greatly improved compared with CPM, especially when the machine is highly saturated. Besides, the calculation time of HFM is theoretically shorter than FEM because HFM only solves a much smaller $N_{mcm} \times N_{mcm}$ matrix, where N_{mcm} represents the number of nodes in the LPMCM.

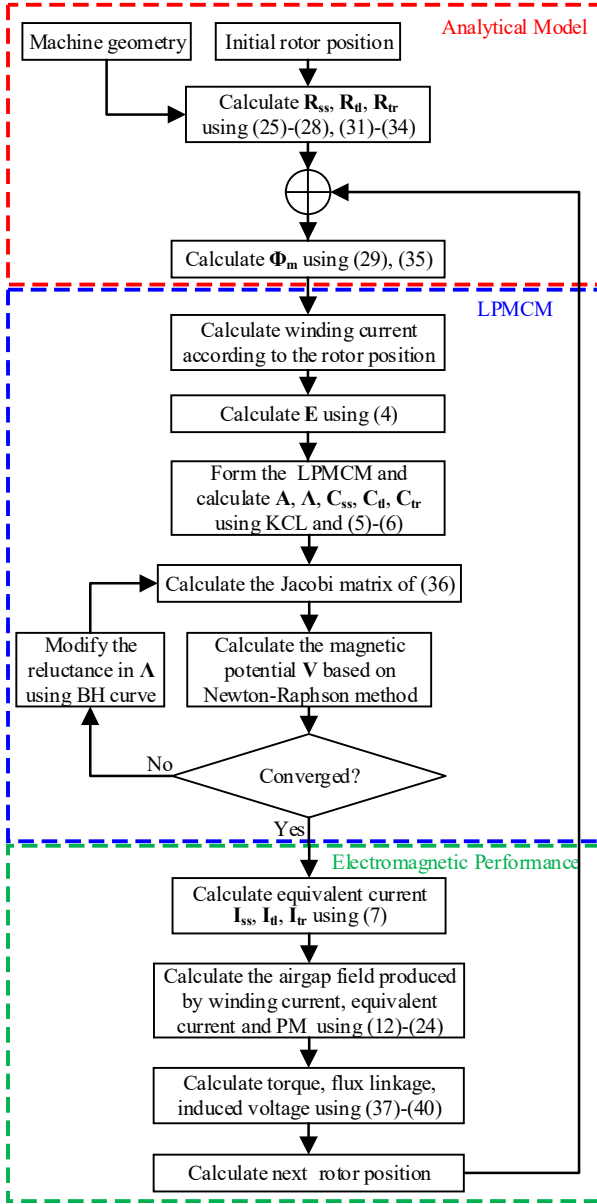


Fig. 7. General flowchart of calculation procedure.

III. ELECTROMAGNETIC PERFORMANCE

The main flux of a coil can be calculated from the airgap field distribution:

$$\varphi_i(t) = R_s I_{ef} \int_{\alpha_i - \tau/2 + b_0/R_s}^{\alpha_i + \tau/2 - b_0/R_s} B_{sr}(\alpha, R_s, t) d\alpha \quad (44)$$

where α_i and τ are the circumferential position and coil pitch of such coil.

By summing the flux linkages associated with all coils from the same phase, the flux linkage ψ_{ph} is derived as:

$$\begin{aligned} \psi_{ph}(t) &= N_c \sum_{i=1}^{\kappa} (\varphi_i(t) + \varphi_l(t)) \\ &= N_c \sum_{i=1}^{\kappa} \left(\varphi_i(t) + \sum_{j=1}^{\gamma} \varphi_{lij}(t) + \sum_{j=1}^{\gamma} \varphi_{l(i+\tau)_j}(t) \right) \end{aligned} \quad (45)$$

where N_c and κ are the number of turns of each coil and the coil number of each phase, respectively. φ_l represents the leakage

flux in all slots and slot openings associated with the phase, which is obtained from the flux distribution in LPMCM. γ is the layer of the tangential magnetic reluctance in one slot. φ_{lij} and $\varphi_{l(i+\tau)_j}$ are the tangential fluxes in the slot that can cover the phase coil [22]. It is also specified in Fig. 4.

The induced voltage is defined as the derivative of the flux linkage with respect to time under on-load condition:

$$U_{ph} = -\frac{d\psi_{ph}}{dt} \quad ph=A,B,C. \quad (46)$$

The electromagnetic torque is determined by the Arkkio's method. It improves Maxwell's stress tensor method, whose accuracy is affected by integration path in the airgap. Therefore, based on the predicted airgap flux density, the total torque is computed by integrating over the surface in the airgap [24]:

$$T = \frac{l_{ef}}{\mu_0(r_s - r_r)} \int_S r B_{sr}(\alpha, r, t) B_{s\alpha}(\alpha, r, t) dS \quad (47)$$

where r and α is the radius and angle of the integration surface element in the airgap. r_s and r_r are the outer and inner radius of the integration surface.

IV. FE AND EXPERIMENTAL VALIDATION

In order to verify the proposed model, the FE analysis have been carried out on two integer-slot (8-pole/48-slot) and fractional-slot (8-pole/9-slot) SPM machines and the experiment has been done on the latter. It is noted that only 2-D FE analysis are performed and therefore the end effect is neglected. The BH curves of iron laminations in the nonlinear FEM for both machines is shown in Fig. 8 while the relative permeability of iron in the linear FEM is 1000000. The differences between nonlinear and linear FEM exhibit the nonlinearity effect. TABLE I gives the major parameters of these two machines. Fig. 9 illustrates that the 8-pole/48-slot machine is operated in the BLAC mode while the other is in the BLDC mode. Fig. 10 gives the field distribution of both SPM machines in the nonlinear FEM, which also reveals the saturation level in the iron. Fig. 11 presents the stator and rotor of 8-pole/9-slot prototype, which is used for experimental validation.

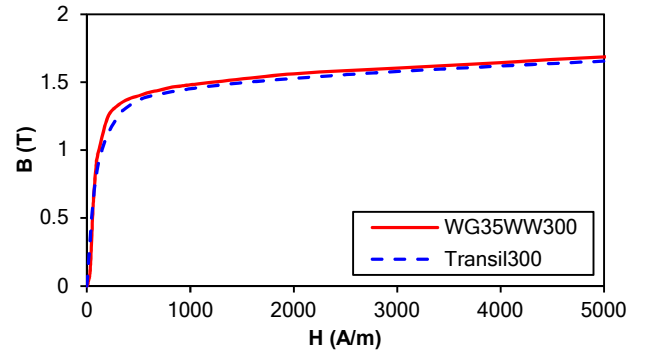
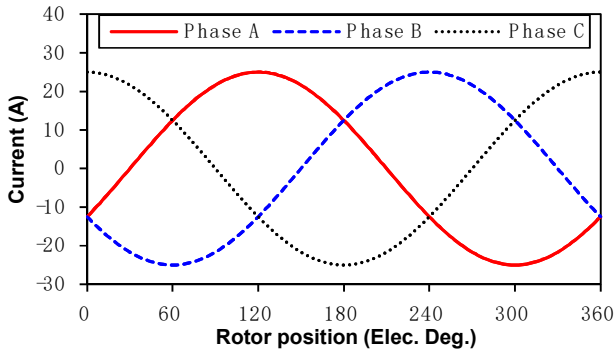


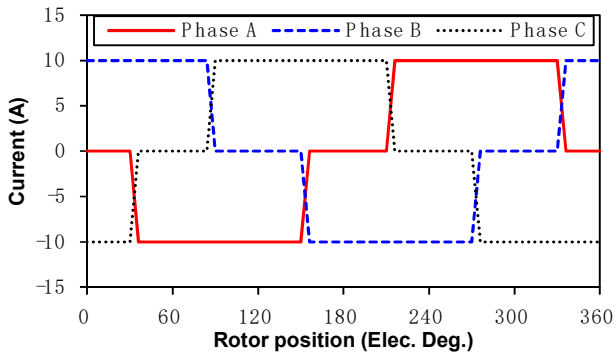
Fig. 8. B-H curves of the iron of both machines.

TABLE I
MAIN PARAMETERS OF PROPOSED SPM MACHINES

Parameter	8-pole/48-slot	8-pole/9-slot	Unit
Stator outer radius	75	50	mm
Stator inner radius	45	26.5	mm
Airgap length	0.75	1	mm
Magnet thickness	4.5	3	mm
Rotor outer radius	44.25	25.5	mm
Shaft radius	17.5	17.5	mm
Stator yoke height	8	4.4	mm
Active length	75	50	mm
Slot opening	1.5	2	mm
Tooth body width	3.72	8.7	mm
Pole-arc to pole-pitch ratio	1	1	
Magnet remanence	1.26	1.2	T
Relative recoil permeability	1.07	1.05	
Magnetization	Parallel	Parallel	
Rated speed	1500	400	rpm
Number of pole pairs	4	4	
Number of slots	48	9	
Rated current (peak)	25	10	A
Lamination material	WG35WW300	Transil300	
Operation mode	BLAC	BLDC	



(a)



(b)

Fig. 9. Current waveforms of the SPM machines at rated load. (a) 8-pole/48-slot. (b) 8-pole/9-slot.

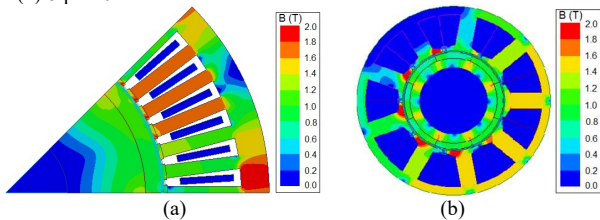


Fig. 10. Flux density distribution of SPM machines at rated current in the nonlinear FEM. (a) 8-pole/48-slot. (b) 8-pole/9-slot.



Fig. 11. 8-pole/9-slot prototype machine. (a) stator (b) rotor.

Under the rated load, the armature reaction field increases the saturation level and HFM becomes more advantageous. Figs. 12-13 show the calculated equivalent current sheet for both machines. Then the airgap field distribution of both machines can be predicted by HFM and compared with CPM and FEM, Figs. 14-15. It can be seen that HFM can accurately predict the airgap flux density while CPM always overestimates due to neglecting nonlinearity effect, especially for the radial airgap flux density facing the fourth tooth of 8-pole/48-slot machine and facing the seventh tooth with 8-pole/9-slot machine. The linear FEM results are also higher than nonlinear FEM results, which shows the influence of iron nonlinearity on the airgap field. Moreover, the average radial airgap flux densities, facing the fourth tooth for the 48-slot machine and facing the seventh tooth for the 9-slot machine, are calculated by HFM, CPM, and FEM at different peak current, as shown in Figs. 16-17. The radial component of HFM predicted flux density agrees well with nonlinear FEM predictions at different peak current while the CPM predicted flux densities are much higher than those predicted by nonlinear FEM but agree well with linear FEM results, as can be seen in both machines. Even under open-circuit condition, the nonlinearity effect exists in both machines to influence the airgap field [22].

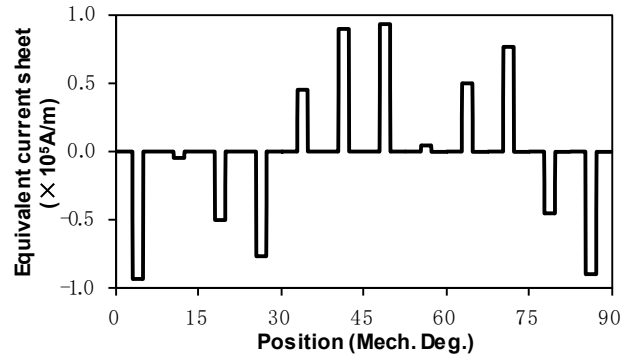


Fig. 12. Equivalent current sheet at stator bore of 8-pole/48-slot SPM machine.

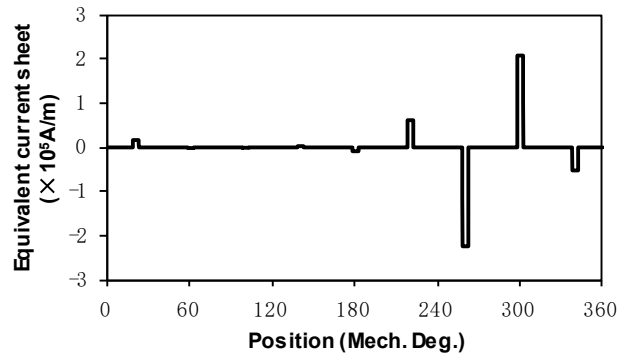


Fig. 13. Equivalent current sheet at stator bore of 8-pole/9-slot SPM machine.

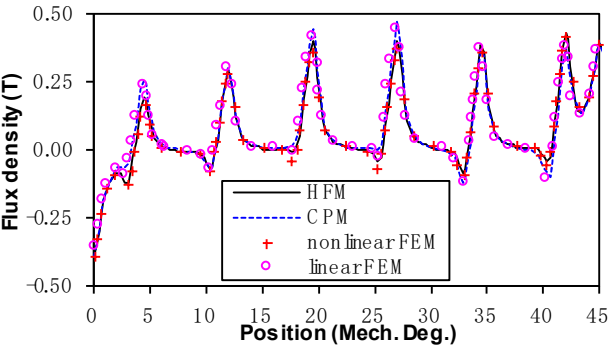
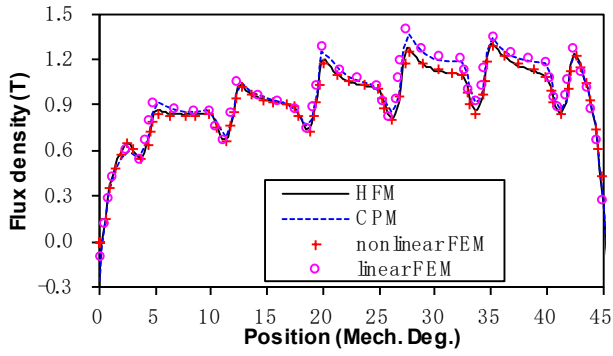


Fig. 14. Comparison of on-load flux densities computed by HFM, CPM, and FE method at the middle airgap of 8-pole/48-slot SPM machine under rated load ($I_{peak}=25A$): (a) radial and (b) circumferential.

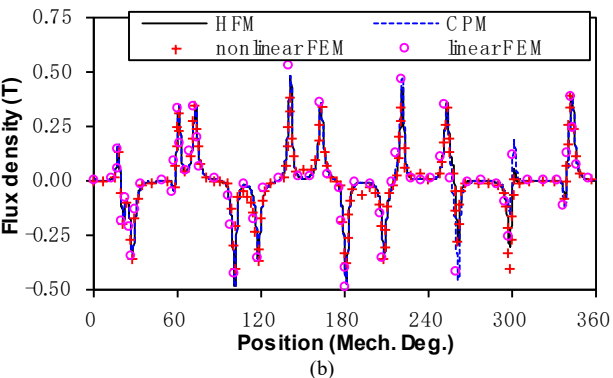
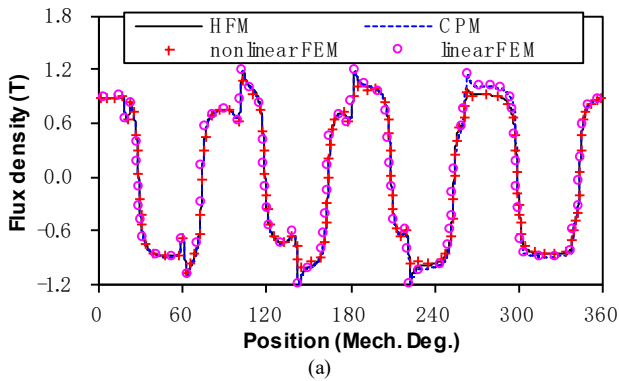


Fig. 15. Comparison of on-load airgap flux densities computed by HFM, CPM, and FE method at the middle airgap of 8-pole/9-slot SPM machine under rated load ($I_{peak}=10A$): (a) radial and (b) circumferential.

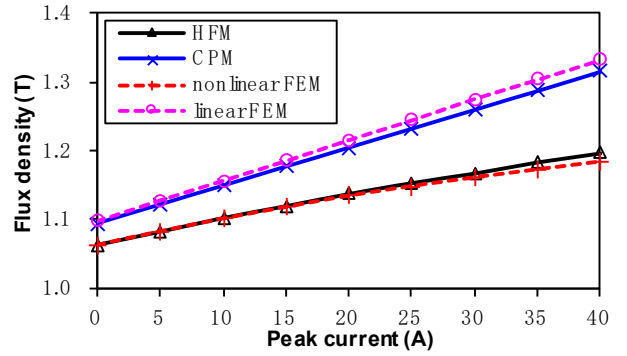


Fig. 16. Variation of average radial airgap flux density facing the fourth tooth with peak current of 8-pole/48-slot SPM machine.

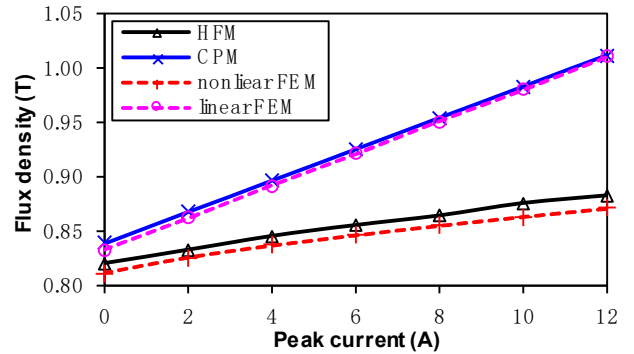


Fig. 17. Variation of average radial airgap flux density facing the seventh tooth with peak current of 8-pole/9-slot SPM machine.

As can be seen in Figs. 18-19, HFM has high accuracy for predicting the induced voltage waveform at rated current while CPM exhibits large errors for both machines. The induced voltage of 8-pole/9-slot machine from Fig. 19 has high surge voltage, because the current waveform in the simulation is ideal and has unsmooth changes. Figs. 20-21 compare the amplitude and phase of the fundamental induced voltage predicted by HFM, CPM and FE Method at different peak current. Again, HFM shows much higher accuracy than CPM. Such advantage of HFM is attribute to its inclusion of flux leakage and nonlinearity effect. Besides, when comparing the nonlinear and linear FEM results from Figs 18-21, it can be seen that the iron nonlinearity has significant influence on the induced voltage.

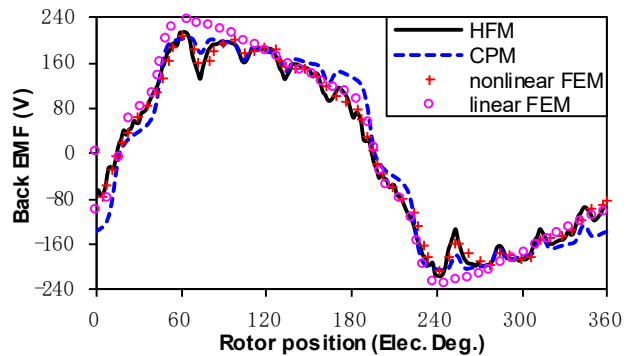


Fig. 18. HFM, CPM, and FE predicted induced voltage waveforms of 8-pole/48-slot SPM machine at rated current.

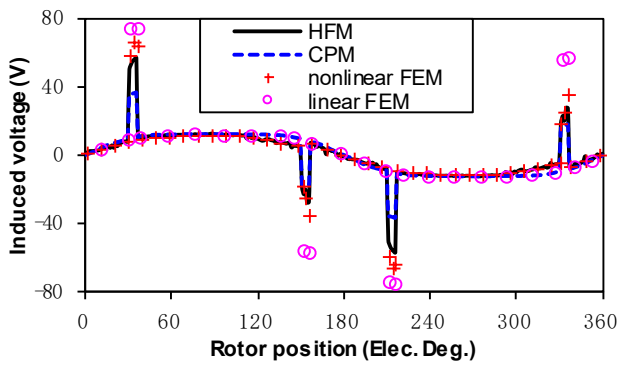


Fig. 19. HFM, CPM, and FE predicted induced voltage waveforms of 8-pole/9-slot SPM machine at rated current.

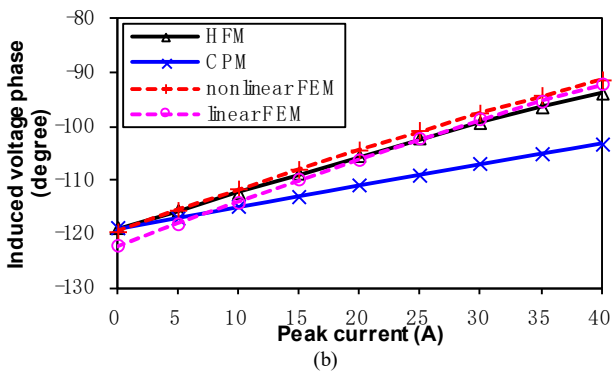
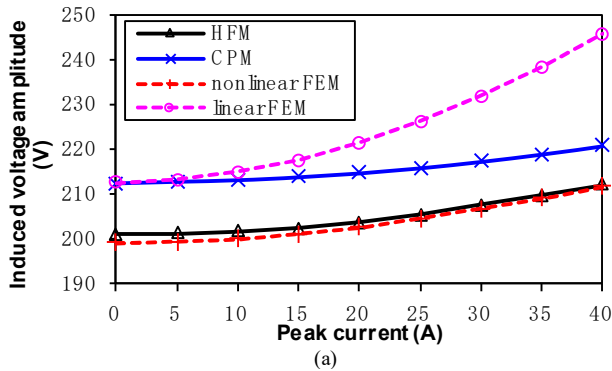


Fig. 20. Variation of amplitude and phase of the fundamental induced voltage with peak current of 8-pole/48-slot SPM machine: (a) amplitude and (b) phase.

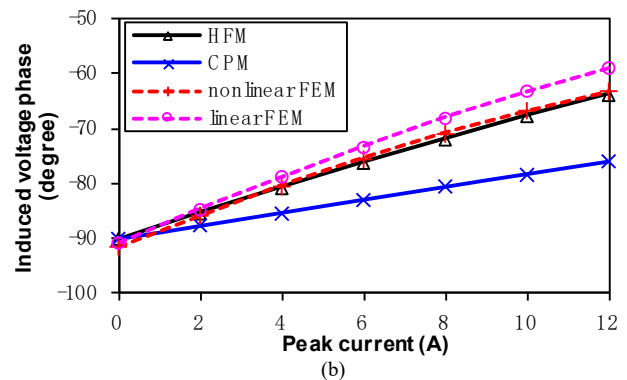
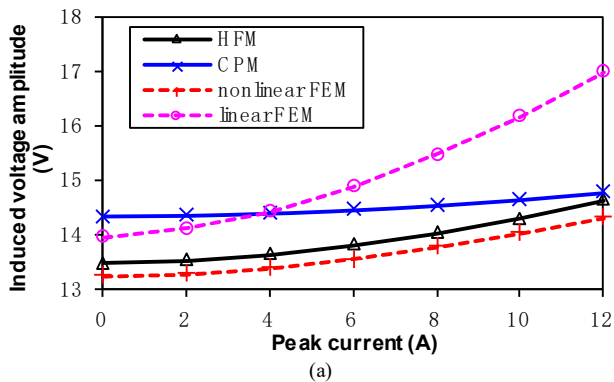


Fig. 21. Variation of amplitude and phase of the fundamental induced voltage with peak current of 8-pole/9-slot SPM machine: (a) amplitude and (b) phase.

As shown in Figs. 22-23, the torque waveform predicted by HFM agrees well with FE prediction at rated current while CPM overestimates it for both machines. The measured torque of 8-pole/9-slot machine also confirms the high accuracy of HFM in Fig. 23. Moreover, as shown in Figs. 24-25, the average torque predicted by HFM achieves excellent accuracy at different load current while the error of CPM prediction gradually becomes larger with the increase of load. It can also be seen from the nonlinear and linear FEM results in Figs. 22-25 that the iron nonlinearity will decrease the torque of SPM machines

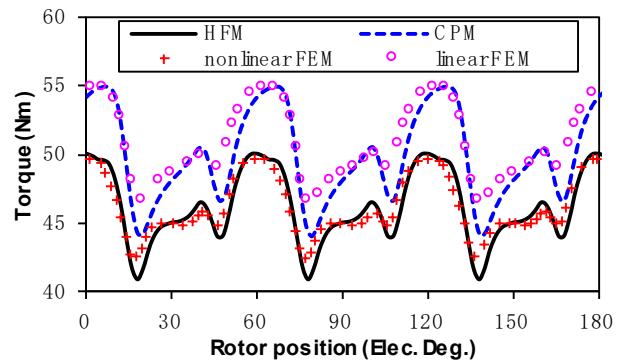


Fig. 22. Torque waveforms of 8-pole/48-slot SPM machine at rated current.

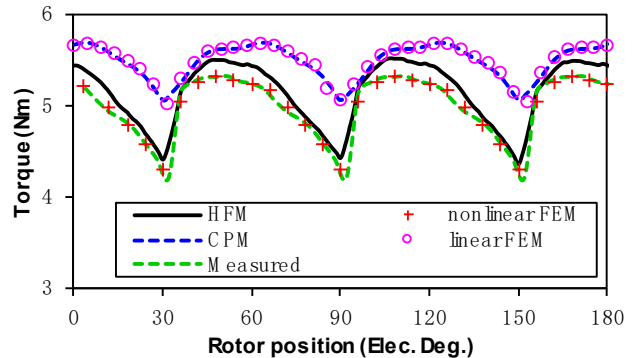


Fig. 23. Torque waveform of 8-pole/9-slot machine at rated current.

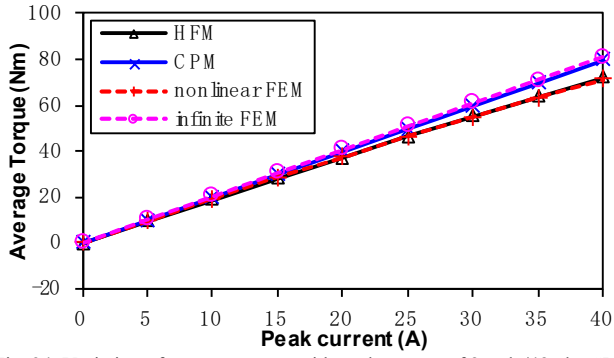


Fig. 24. Variation of average torque with peak current of 8-pole/48-slot SPM machine.

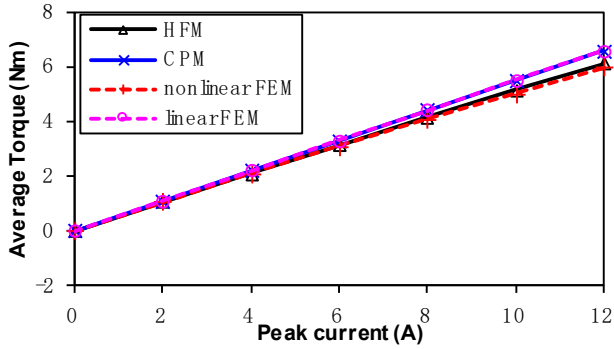


Fig. 25. Variation of average torque with peak current of 8-pole/9-slot SPM machine.

In order to compare the computational speed of HFM, CPM, and nonlinear FEM, their calculation time in one electric period for both machines is compared and analyzed in TABLE II and TABLE III. It is noted that FEM results of both machines are solved in Ansys Maxwell while CPM and HFM calculations are performed in Matlab. The main parameter setting of simulation is shown in TABLE IV. It can be seen that CPM is the fastest while FEM is the slowest for both machines. HFM calculation runs at least ten times faster than FEM simulation for both machines. This advantage will significantly improve the efficiency of machine design.

TABLE II
CALCULATION TIME OF 8-POLE/48-SLOT SPM MACHINE

Model	Current (A)								
	0	5	10	15	20	25	30	35	40
CPM	1.1	1.0	1.0	1.1	1.0	1.0	1.0	1.0	1.0
HFM	50.3	42.4	41.5	38.5	38.0	44.3	48.2	44.3	43.8
FEM, nonlinear	537	534	579	577	537	535	543	550	541

TABLE III
CALCULATION TIME OF 8-POLE/9-SLOT SPM MACHINE

Model	Current (A)						
	0	2	4	6	8	10	12
CPM	1.8	1.8	1.7	1.6	1.6	1.7	1.7
HFM	44.9	44.9	43.3	42.2	43.7	44.2	45.0
FEM, nonlinear	650	671	637	679	672	652	657

TABLE IV
MAIN PARAMETER SETTING OF SIMULATION

Machine model	Airgap segment	Simulation steps	node
8-pole/ 48-slot	CPM	720	0
	HFM		120
	FEM		17965
8-pole/ 9-slot	CPM	480	0
	HFM		90
	FEM		33035

V. CONCLUSION

A hybrid field model integrating CPM and LPMCM has been developed for analyzing SPM machines considering nonlinearity effect and tooth-tips. The nonlinearity of the stator yoke and tooth body is represented by equivalent current on the slot opening while the tooth-tip saturation is accounted for by additional equivalent current sheet on the tooth surface. Based on such equivalent currents, the permeability of the iron can be regarded as infinite and superposition theory can be applied to calculate the on-load airgap field produced by PMs, winding and equivalent currents. In order to calculate the equivalent current, a solving procedure is introduced to guarantee the convergence. Then the airgap field distribution, induced voltage and torque are all obtained from HFM. HFM has higher accuracy than CPM in predicting the airgap field and electromagnetic performance when the iron material in the machine works around the nonlinear region. It is demonstrated by both FE analysis and experiment. Based on HFM, other machines such as inset PM machines and IPM machines will be investigated in the future.

ACKNOWLEDGMENT

This work was supported by the National Natural Science Foundation of China under Grant 51677169 and Grant 51637009 and by the Fundamental Research Funds for the Central Universities under Grant 2017QNA4016.

REFERENCES

- [1] Z. Q. Zhu and D. Howe, "Electrical machines and drives for electric, hybrid, and fuel cell vehicles," *Proc. IEEE*, vol. 95, no. 4, pp. 746-765, Apr. 2007.
- [2] S. Ruoho, T. Santa-Nokki, J. Kolehmainen, and A. Arkkio, "Modeling magnet length in 2-D finite-element analysis of electric machines," *IEEE Trans. Magn.*, vol. 45, no. 8, pp. 3114-3120, Aug. 2009.
- [3] Z. Q. Zhu, D. Howe, E. Bolte, and B. Ackermann, "Instantaneous magnetic field distribution in brushless permanent magnet dc motors. Part I: open-circuit field," *IEEE Trans. Magn.*, vol. 29, no. 1, pp. 124-135, Jan. 1993.
- [4] Z. Q. Zhu and D. Howe, "Instantaneous magnetic field distribution in brushless permanent magnet DC motors. II. armature-reaction field," *IEEE Trans. Magn.*, vol. 29, no. 1, pp. 136-142, Jan. 1993.
- [5] D. Zarko, D. Ban, and T. A. Lipo, "Analytical calculation of magnetic field distribution in the slotted air gap of a surface permanent-magnet motor using complex relative air-gap permeance," *IEEE Trans. Magn.*, vol. 42, no. 7, pp. 1828-1837, July 2006.
- [6] T. C. O'Connell and P. T. Krein, "A Schwarz-Christoffel-based analytical method for electric machine field analysis," *IEEE Trans. Energy Convers.*, vol. 24, no. 3, pp. 565-577, Sept. 2009.

- [7] K. Boughrara, R. Ibtiouen, D. Zarko, O. Touhami, and A. Rezzoug, "Magnetic field analysis of external rotor permanent-magnet synchronous motors using conformal mapping," *IEEE Trans. Magn.*, vol. 46, no. 9, pp. 3684-3693, Sept. 2010.
- [8] K. Ramakrishnan, D. Zarko, A. Hanic, and G. Mastinu, "Improved method for field analysis of surface permanent magnet machines using Schwarz-Christoffel transformation," *IET Electr. Power Appl.*, vol. 11, no. 6, pp. 1067-1075, July 2017.
- [9] L. J. Wu, Z. Q. Zhu, D. Staton, M. Popescu, and D. Hawkins, "An improved subdomain model for predicting magnetic field of surface-mounted permanent magnet machines accounting for tooth-tips," *IEEE Trans. Magn.*, vol. 47, no. 6, pp. 1693-1704, June 2011.
- [10] T. A. Driscoll, Schwarz-Christoffel Toolbox User's Guide: Version 2.3, 2005.
- [11] V. Ostovic, *Dynamics of saturated electric machines*. New York, NY, USA: Springer-Verlag, 1989.
- [12] X. Huang, M. Zhu, W. Chen, J. Zhang and Y. Fang, "Dynamic reluctance mesh modeling and losses evaluation of permanent magnet traction motor," *IEEE Trans. Magn.*, vol. 53, no. 6, pp. 1-4, Jun. 2017.
- [13] A. Dalal and P. Kumar, "Analytical model for permanent magnet motor with slotting effect, armature reaction, and ferromagnetic material property," *IEEE Trans. Magn.*, vol. 51, no. 12, pp. 1-10, Dec. 2015.
- [14] F. R. Alam and K. Abbaszadeh, "Magnetic field analysis in eccentric surface-mounted permanent-magnet motors using an improved conformal mapping method," *IEEE Trans. Energy Convers.*, vol. 31, no. 1, pp. 333-344, March 2016.
- [15] K. Abbaszadeh and F. Rezaee Alam, "On-load field component separation in surface-mounted permanent-magnet motors using an improved conformal mapping method," *IEEE Trans. Magn.*, vol. 52, no. 2, pp. 1-12, Feb. 2016.
- [16] F. Rezaee Alam, B. Rezaeecalum, and J. Faiz, "Unbalanced magnetic force analysis in eccentric surface permanent-magnet motors using an improved conformal mapping method," *IEEE Trans. Energy Convers.*, vol. 32, no. 1, pp. 146-154, Mar. 2017.
- [17] L. Zhu, S. Z. Jiang, Z. Q. Zhu, and C. C. Chan, "Analytical modeling of open-circuit air-gap field distributions in multisegment and multilayer interior permanent-magnet machines," *IEEE Trans. Magn.*, vol. 45, no. 8, pp. 3121-3130, Aug. 2009.
- [18] J. R. Anglada and S. M. Sharkh, "Analytical calculation of the torque produced by transverse flux machines," *IET Electr. Power Appl.*, vol. 11, no. 7, pp. 1298-1305, August, 2017.
- [19] P. Jalali, S. T. Boroujeni, and N. Bianchi, "Analytical modeling of slotless eccentric surface-mounted PM machines using a conformal transformation," *IEEE Trans. Energy Convers.*, vol. 32, no. 2, pp. 658-666, June 2017.
- [20] A. Hanic, D. Zarko, and Z. Hanic, "A novel method for no-load magnetic field analysis of saturated surface permanent-magnet machines using conformal mapping and magnetic equivalent circuits," *IEEE Trans. Energy Convers.*, vol. 31, no. 2, pp. 740-749, Jun. 2016.
- [21] A. Hanic, D. Zarko, D. Kuhinek, and Z. Hanic, "On-Load analysis of saturated surface permanent magnet machines using conformal mapping and magnetic equivalent circuits," *IEEE Trans. Energy Convers.*, vol. 33, no. 3, pp. 915-924, Sept. 2018.
- [22] L. J. Wu, Z. K. Li, X. Y. Huang, Y. L. Zhong, Y. T. Fang, and Z. Q. Zhu, "A hybrid field model for open-circuit field prediction in surface-mounted PM machines considering saturation," *IEEE Trans. Magn.*, vol. 54, no. 6, pp. 1-12, June 2018.
- [23] Z. Q. Zhu, D. Howe, and C. C. Chan, "Improved analytical model for predicting the magnetic field distribution in brushless permanent-magnet machines," *IEEE Trans. Magn.*, vol. 38, no. 1, pp. 229-238, Jan 2002.
- [24] A. Arkkio, "Analysis of Induction Motors Based on the Numerical Solution of the Magnetic Field and Circuit Equations", Acta Polytechnica Scandinavica, Electrical Engineering Series, no. 59, pp. 97, 1987.
- [25] L. J. Wu, Z. Q. Zhu, D. A. Staton, M. Popescu, and D. Hawkins, "Comparison of analytical models of cogging torque in surface-mounted PM machines," *IEEE Trans. Ind. Electron.*, vol. 59, no. 6, pp. 2414-2425, June 2012.
- [26] Z. Azar, Z. Q. Zhu, and G. Ombach, "Influence of electric loading and magnetic saturation on cogging torque, back-EMF and torque ripple of PM machines," *IEEE Trans. Magn.*, vol. 48, no. 10, pp. 2650-2658, Oct. 2012.
- [27] Z. Q. Zhu and D. Howe, "Instantaneous magnetic field distribution in permanent magnet brushless DC motors. IV. magnetic field on load," *IEEE Trans. Magn.*, vol. 29, no. 1, pp. 152-158, Jan. 1993.
- [28] P. Jalali, S. Taghipour Boroujeni, and N. Bianchi, "Simple and efficient model for slotless eccentric surface-mounted PM machines," *IET Electr. Power Appl.*, vol. 11, no. 4, pp. 631-639, April 2017.